Quantum structures for multiband photon detection

A.G.U. PERERA

Department of Physics and Astronomy, Georgia State University, Atlanta, GA 30303, USA

The work describes multiband photon detectors based on semiconductor micro- and nano-structures. The devices considered include quantum dot, homojunction, and heterojunction structures. In the quantum dot structures, transitions are from one state to another, while free carrier absorption and internal photoemission play the dominant role in homo or heterojunction detectors. Quantum dots-in-a-well (DWELL) detectors can tailor the response wavelength by varying the size of the well. A tunnelling quantum dot infrared photodetector (T-QDIP) could operate at room temperature by blocking the dark current except in the case of resonance. Photoexcited carriers are selectively collected from InGaAs quantum dots by resonant tunnelling, while the dark current is blocked by AlGaAs/InGaAs tunnelling barriers placed in the structure. A two-colour infrared detector with photoresponse peaks at ~6 and ~17 µm at room temperature will be discussed. A homojunction or heterojunction interfacial workfunction internal photoemission (HIWIP or HEIWIP) infrared detector, formed by a doped emitter layer, and an intrinsic layer acting as the barrier followed by another highly doped contact layer, can detect near infrared (NIR) photons due to interband transitions and mid/far infrared (MIR/FIR) radiation due to intraband transitions. The threshold wavelength of the interband response depends on the band gap of the barrier material, and the MIR/FIR response due to intraband transitions can be tailored by adjusting the band offset between the emitter and the barrier. GaAs/AlGaAs will provide NIR and MIR/FIR dual band response, and with GaN/AlGaN structures the detection capability can be extended into the ultraviolet region. These detectors are useful in numerous applications such as environmental monitoring, medical diagnosis, battlefield-imaging, space astronomy applications, mine detection, and remote-sensing.

Keywords: multicolour, dual band, infrared detectors, quantum dot (QD), quantum well (QW).

1. Introduction

Detecting an object's infrared emission at multiple wavelengths can be used to eliminate surface and shape effects and reconstruct the object temperature. However, measuring multiple wavelength bands typically requires multiple detectors with separate cooling assemblies and electronics. The difficulties of assembling several detectors and the increased cost can be overcome by using a single detector responding in multiple bands. This article discusses detectors that are sensitive to multiple wavelength bands. These can be used in applications such as mine detection [1], where the number of false positives can be reduced by multiband approach. Also the NIR portion of a NIR/FIR dual band detector could be used to detect the muzzle flash to locate the position of enemy troops, while the FIR radiation is useful for locating troops and operating vehicles. Moreover, a multiband detector can be used as a remote thermometer by taking the difference of the signal for the two bands, and in other applications such as environmental monitoring, medical diagnostics, battlefield-imaging, and space astronomy applications.

2. Quantum dots-in-a-well infrared detectors

Quantum dot infrared photodetector (QDIP) research has attracted much attention for mid-wave and long-wave infrared applications [2–5] during past few years. Several research groups have already demonstrated the intersubband transitions in mid-infrared (MIR) and far-infrared (FIR) QDIPs [6].

Owing to the three-dimensional confinement of carriers, QDIPs are sensitive to normal-incidence infrared radiation, which is forbidden in n-type quantum well infrared photo detectors (QWIPs). In addition, QDIPs are expected to show improved performance characteristics such as low dark current and higher operating temperatures [2,7–10]. In a quantum dots-in-a-well (DWELL) structure, the InAs dots are placed in a thin InGaAs quantum well, which in turn is positioned in a GaAs matrix [5]. The DWELL heterostructure provides a better confinement for carriers trapped in the quantum dot by lowering the ground state of the dot with respect to the GaAs band edge resulting in low thermionic emission. Here, the experimental results on three-colour detector structures with different quantum well widths are reported, discussing the transitions leading to each peak.

2.1. Device structure and experiment

The DWELL detectors were grown in a VG-80 solid source molecular beam epitaxy system with a cracked As$_2$ source. The GaAs layers were grown at a substrate temperature, T_{sub} = 580°C whereas the In$_{0.15}$Ga$_{0.85}$As well and the InAs dots were grown at T_{sub} = 480°C as measured by an optical pyrometer. Using standard lithography, metal evaporation and wet etching, n-i-n detectors were fabricated for top-side illumination. The diameter of the optically active area varied from 25–300 µm. The design for the detector structure 1388 is shown in Fig. 1(a). The other two detectors are identical except for the thickness of InGaAs well layer. There are ten layers of n-doped InAs/In$_{0.15}$Ga$_{0.85}$As in each of the detector structure. The QDs are directly doped n-type using Silicon as the dopant to a sheet density of 5×10^{11} cm^2, which corresponds to about 1 electron per dot, while the QW is not intentionally doped. Square mesa devices 400 µm on a side were processed, and a 300-µm diameter opening was left in the top contact for frontside illumination. From photoluminescence measurements of the ground state transition of the dot (1.25 µm at T = 300 K) and using a 60:40 conduction: valence band ratio, it is estimated that the ground state of the dot is about 250 meV below the GaAs band edge. There can be at least two bound states in the dot and one confined state in the quantum well [11], as shown in Fig. 1(b). The detectors were processed, wire bonded to chip carriers, and spectral response was obtained for normal incidence radiation using a Perkin Elmer System 2000 Fourier Transform Infrared (FTIR) spectrometer, and calibrated by a background spectra obtained with a Si composite bolometer with the same set of optical components.

2.2. Results and discussion

The three detectors [12] (1299, 1373, and 1388) described here had the same parameters except the width of the well (90 Å, 110 Å, and 120 Å, respectively), and each responds at three distinct wavelengths. The spectral response of the three detectors in the range 3–15 µm is shown in Fig. 2. The two curves for each detector in the figure are for two different bias values (–0.5 V and –1.4 V). All three detectors have two distinct peaks in the MIR range. Sample 1299 exhibits its first peak at ~4.2 µm and the second peak at ~8.1 µm. A semi-empirical estimate, based on the photoluminescence spectra with a 60:40 split of the bandgap difference, gives the energy separation between the ground state of the dot and conduction band edge of the GaAs barrier to be 225–250 meV (~4.9–5.5 µm). Hence, the 4.2 µm peak is probably due to transitions from the ground state of the dot to the continuum state of the well and the second peak should be due to transitions from the ground state of the dot to a bound state in the well as shown in the inset to Fig. 2. Moreover, it has been shown [13] that the line width ($\Delta\lambda/\lambda$) of quantum well detector transitions from bound to bound states is narrower than that of transitions from bound to continuum states. The line width (full width half maximum) of 4.2-µm peak is about 42% whereas the line width of 8.1-µm peak is about 28%, consistent with the above description. The photocurrent is proportional to the product of the oscillator strength and the escape probability. For the bound-to-bound peak, the oscillator strength is larger whereas the escape probability is smaller, and for the bound-to-continuum peak, the oscillator strength is smaller whereas the escape probability is larger, and does not depend as much on the bias. Hence, the bound-to-continuum peak is seen even at lower biases whereas the bound-to-bound peak dominates at larger biases, where field assisted tunnelling increases the escape probability.

When the width of the quantum well is increased, the energy spacing between the levels in the well decreases causing the second MIR peak to red-shift since it is connected to transitions from the dot to well bound state. However, the shift of the first peak of 1373 is more compli-
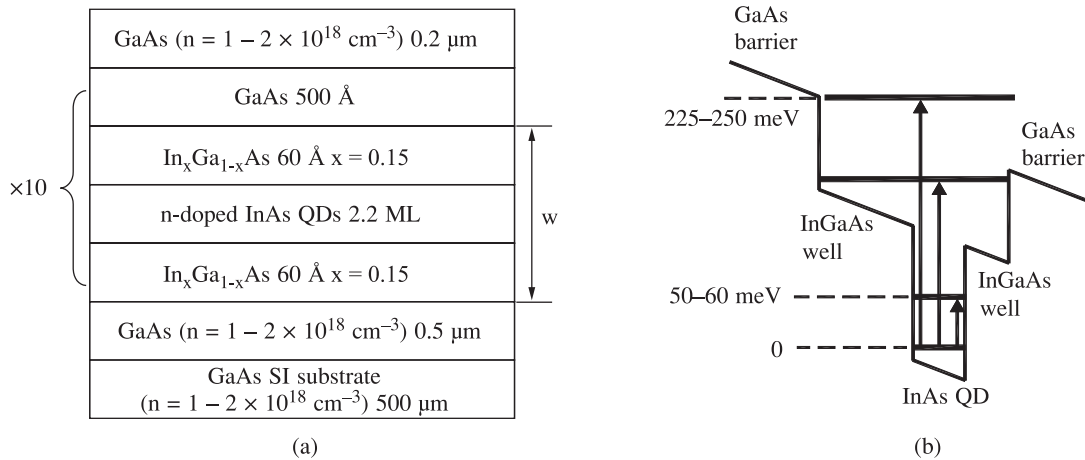

Fig. 1. The schematics of the dots-in-a- well detector structure as grown. The width of the quantum well, i.e. the combined width of the InGaAs layers (indicated as *w* in the figure), is deferent for each detector. Structures 1299, 1373, and 1388 have well widths of 90, 110, and 120 Å respectively, while all other parameters are the same (a). The conduction band profile of the DWELL structure with the energy states corresponding to possible transitions leading to spectral response (b).
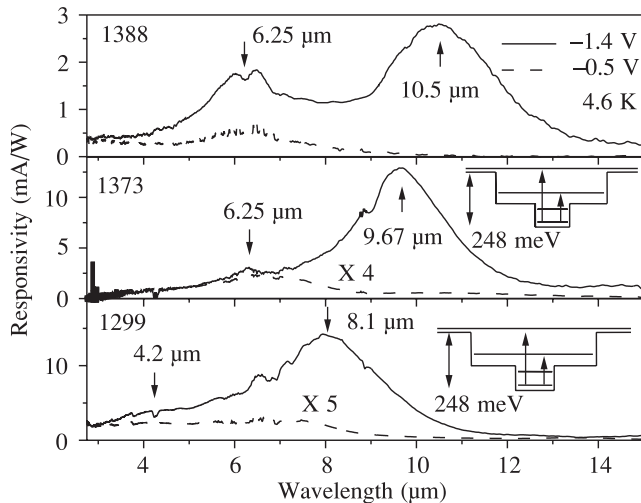
Fig. 2. The first two peaks of the three detectors at 4.6 K under −1.4 V and −0.5 V bias. The band diagram showing the transitions leading to each peak is given in the inset and the transition states for 1388 are the same as 1373. Arrows indicate the peak positions and × sign implies that the curve has been multiplied by the number indicated.

cated. The continuum state in 1299 could become quasi-bound state in both 1373 and 1388 since the 1373, and 1388 detectors are made by stretching the well of 1299. Then, the first peaks of 1373 and 1388 are due to transitions from the ground state of the dot to a quasi-bound state in the well. This can be confirmed by the red-shift of the first peaks of 1373, and 1388 and the narrower line width compared with 1299. As designed, the first peak of 1373 is expected in between the first peak of 1299 and 1388. However, it is almost at the same position of the first peak of 1388 and the second peak of 1373 is closer to that of 1388 than expected. This could be explained if the size of the quantum dot of 1373 was unintentionally changed during the growth process.

The spectral responsivity of the third peak of 1388 in FIR region under different applied bias fields is shown in Fig. 3(a). From 8-band $k \cdot p$ modelling [14], it is found that the energy separation between the states in the QDs with base diameter of 20 nm and height of 7–8 nm is about 50–60 meV. The FIR peak at ~23.3 μm (53.2 meV) is due to transitions between two bound states in the dot. An energy level diagram corresponding to this transition is shown in the inset to Fig. 3(a). The variation of the peak responsivity of 23.3 μm peak with the bias voltage is given in Fig. 3(b). As shown in the energy band diagrams, carriers excited to the bound state from the ground state in the dot at low fields still have to tunnel through the well and barrier region to reach the continuum, and be collected by the external circuit. At higher fields, the barrier is pulled strongly down so that the excited carriers have to tunnel only through thin regions of well and barriers. This would lead to field-assisted tunnelling, increasing the escape probability. As a result, the experimental response curves show a drastic increase in the response when the bias is increased from −1.0 V to −2.4 V. Moreover, the FIR peak is broader than a peak expected from bound-to-bound transitions, and it is possibly due to the 10% size fluctuations of the dots. This is also reflected in the broader PL line width of QDs compared to that of the QWs.

The variation of the dark current density of samples 1299, 1373, and 1388 with bias voltage at 77 K is shown in Fig. 4. The symmetry observed for 1388 compared with other two samples is due to the symmetry of the structure. In 1388, the dots are placed symmetrically in the well. That is the two well layers have the same thickness. But for 1373, and 1299, the thicknesses of the two InGaAs well layers are different, making an asymmetric structure. Among all these detectors, 1388 showed the lowest dark current, and hence the highest detectivity of ~7.9×10^{10} Jones at 4.6 K under −2.2 V bias and 3.2×10^{10} Jones at 80
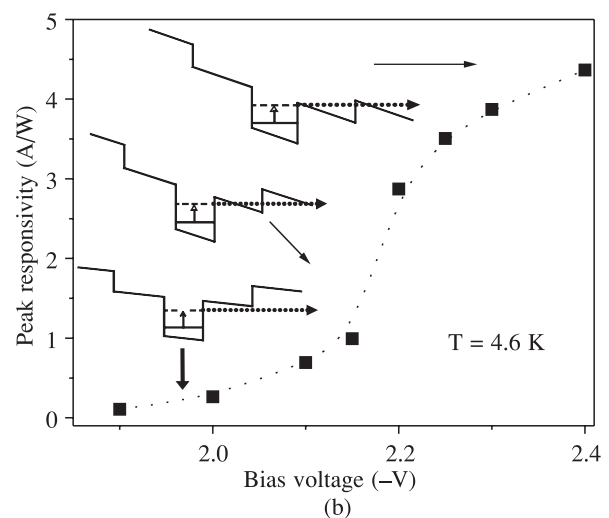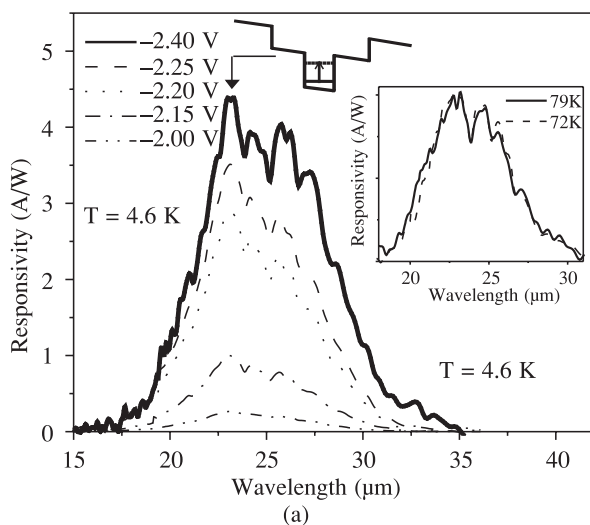

Fig. 3. The FIR response of 1388 at different bias values (negative indicates that the top contact is negative). The band diagram represents the transition leading to the response. The inset shows the responsivity at high temperature (72 K and 79 K) (a). The variation of the peak responsivity of 1388 detector with applied bias and the corresponding transition between the states in the dot with bias (b).
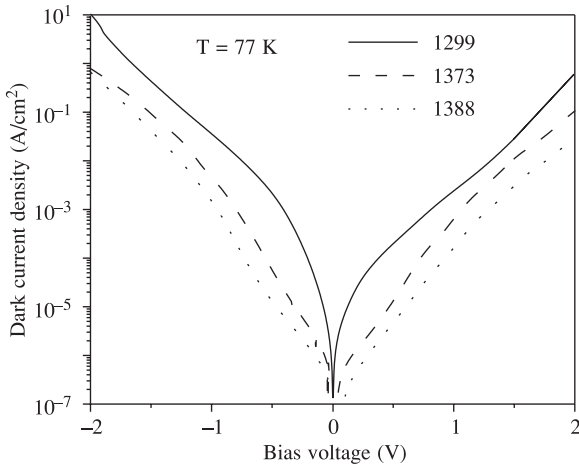
Fig. 4. The variation of the dark current density of samples 1299, 1373, and 1388 with bias voltage at 77 K. The symmetry observed for 1388 compared with other two samples is due to the symmetry of the structure. In 1388, the dot is placed symmetrically in the well, while in 1299, and 1373, the dot is not placed at the centre of the well.

K under –1.4 V bias was reported at 23.3 μm wavelength. All but the FIR peak of 1373 were observed up to 80 K while the FIR peak of 1373 could be obtained up to 60 K. A GaAs/AlGaAs QWIP broadband detector, sensitive in 10–16 μm spectral range with a detectivity of ~10^{10} at 55 K, has been reported by Bandara *et al*. [15] The improvement in the operating temperature of FIR response of DWELL detectors (up to 80 K), compared with a typical FIR QWIP [16] operating at ~10–20 K, proves the benefit of the quasi-zero dimensional confinement.

According to the experimental results [12], the FIR peak stays almost at the same position (~23.3 μm) for sample, 1299 and 1388. Changing the width of the quantum well does not affect states in the quantum dot and this confirms

that the FIR peak is due to transitions between dot states. Due to the fact that the dot size of 1373 has been increased causing the energy difference between dot states to decrease, the FIR peak of 1373 has shifted to ~25.5 μm. The three peaks of DWELL detectors are expected to respond differently to polarized radiation. Hence, the energy states, and the transitions leading to each peak of DWELL detectors can be further explained by polarization measurements.

3. Tunnelling quantum-dot infrared photodetector (T-QDIP)

So far, the conventional QD IR detectors have not shown drastic temperature improvements, increasing the cost of making cameras with traditional cooling systems. Therefore, the operating temperature is a very significant issue, and developing an IR detector operating at room temperature has become important.

Even for QDIPs, the electron occupation is dominated by excited states at temperatures above 150 K [17]. Therefore, in the conventional QDIP, the reduction of the dark current is not significant at temperatures above 150 K. In general, any device structure designed to reduce the dark current, reduces the photocurrent as well. A novel approach, the tunnelling QDIP shown in Fig. 5(b) uses resonant tunnelling to selectively collect the photocurrent generated within the quantum dots, while the same tunnelling barriers block the carriers contributing to the dark current. Furthermore, in these devices, polarization selection rules allow absorption of normal incidence light; and a long effective carrier lifetime, ~100's of picoseconds, confirmed by theory [18] and experiments [19], provides the potential for large responsivity. Here, a room temperature T-QDIP, showing two colour responses at wavelengths of ~6 and ~17 μm is discussed.
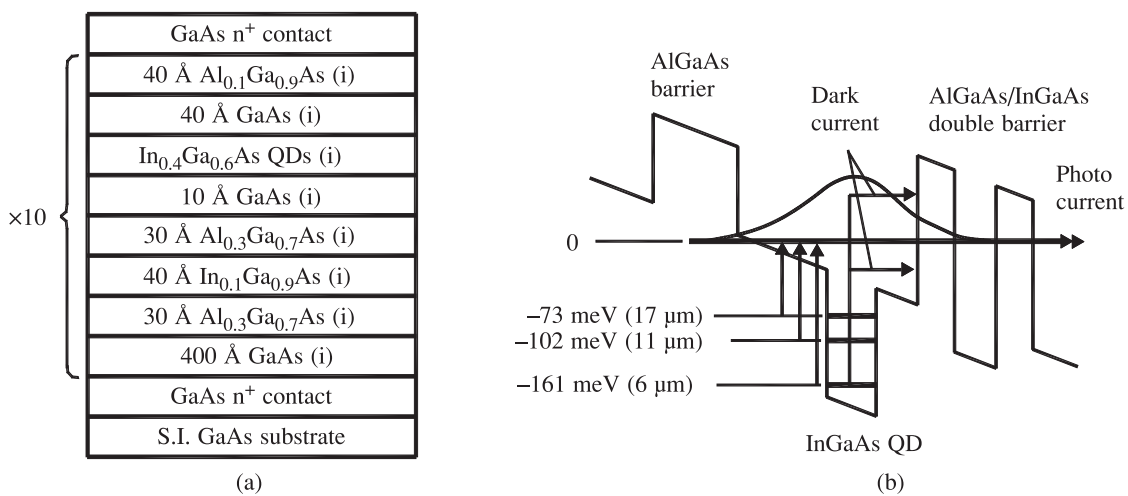

Fig. 5. Schematic heterostructure of a T-QDIP grown by molecular beam epitaxy. InGaAs QDs are placed in a GaAs well. The AlGaAs/InGaAs/AlGaAs layers serve as a double-barrier to decouple the dark and photo currents. The letter i indicates that the layer is intrinsic (a). Schematic diagram of the conduction band profile of the tunnelling QDIP (T-QDIP) under reverse applied bias along with the calculated bound state energies in the dot and the well. The dark current channels are blocked by the barrier unless they happen to be excited to match the resonance level (b).

3.1. Device structure

The T-QDIP structure, grown by molecular beam epitaxy, is schematically shown in Fig. 5(a). The GaAs and AlGaAs layers were grown at 610°C and the quantum dot layers were grown at 500°C. Vertical circular mesa for top illuminations were fabricated by standard photolithography, wet chemical etching and contact metallization techniques. The n-type top ring contact and the bottom contact were formed by evaporated Ni/Ge/Au/Ti/Au with thickness of 50/325/650/200/2000 Å. The radius of the optically active area varies from 100–300 µm. Devices for testing are mounted on to chip carriers with silver epoxy and gold wire contacts were made from the device to the chip carrier leads.

Figure 5(b) shows the band diagram under an applied reverse bias. The double-barrier resonant tunnelling heterostructure serves to decouple the dark- and photocurrents. A single $Al_{0.1}Ga_{0.9}As$ barrier has been introduced on the other side of the dot to create a quantum well, in which well-defined quasi-bound final states are available for photo-excited electrons. The structure is designed so that these states resonate with the tunnelling states in the $In_{0.1}Ga_{0.9}As/Al_{0.3}Ga_{0.7}As$ double barrier system. For photoexcited carriers with energy equal to the energy difference between QD bound state and well final state, the tunnelling probability is near unity as confirmed by calculations. The energy states in the quantum dot, and the well were calculated by an eight-band $k \cdot p$ model [20], and solving the one dimensional Schrödinger equation including the presence of the wetting layer, respectively.

3.2. Results and discussion

The variation of the dark current density with the voltage in the temperature range 240–300 K, is shown in Fig. 6(a). The dark current densities at a bias of 1 V are 0.21, 0.96, and 1.55 A/cm² at 240, 280, and 300 K, respectively. These are lower than the dark current of other infrared detectors measured at these temperatures. For DWELL reported in this article, the best dark current density, reported for 1388 as shown in Fig. 4, is ~1.7×10⁴ A/cm², while T-QDIP reported a dark current density of ~4.3×10⁹ A/cm² at 77 K under 1-V bias.

Figure 6(b) shows the spectral response measured with an applied bias of –2 V in the temperature range 240–300 K, and the inset shows the responsivity at 80 K under –3 V bias. There are two distinct peaks observed at high temperature, centred around ~6 and ~17 µm, and a weak response around 11 µm. In addition, as seen in the responsivity curve at 80 K, the 6-µm peak has split in to two closely spaced peaks at 5.7 and 6.2 µm. These arise from the overlapping of the wave functions of the quantum well states and the bound states of the double barrier heterostructure. The 6-µm peak has a peak responsivity of ~0.75 A/W, and 16% quantum efficiency under optimum conditions. The peak responsivity of the long wavelength peak at 17 µm is 0.032 A/W at 300 K, and it is dominant at 300 K. The peak at ~6 µm is due to transitions from the ground state of the dot to the quasi-bound state in the well ($\Delta E = 161$ meV), whereas the 17-µm peak results from transitions from the second excited state of the dot to the quasi-bound state ($\Delta E = 73$ meV) in the well, as shown in Fig. 5(b). The line width of this transition is ~26 meV, and it is corresponding to the inhomogeneous broadening of the QD states at 300 K. Due to the symmetry of the dot geometry, the excited states in the QD have a higher degeneracy (8) than the ground state (2). Therefore the number of carriers in the excited states compared to that in the ground state increases with the temperature although the occupation probability is lower. As a result, the 17-µm peak is dominant at high temperatures. The weak response at ~11 µm corresponds to the energy separation between the first excited dot state and the well state ($\Delta E = 102$ meV). Furthermore, the specific detectivity, D^*, at 17 µm is on the order of 10⁷ Jones at 300 K, and with some re-designing of the device heterostructure, $D^* \sim 10^9$ Jones can be achieved under the same conditions.
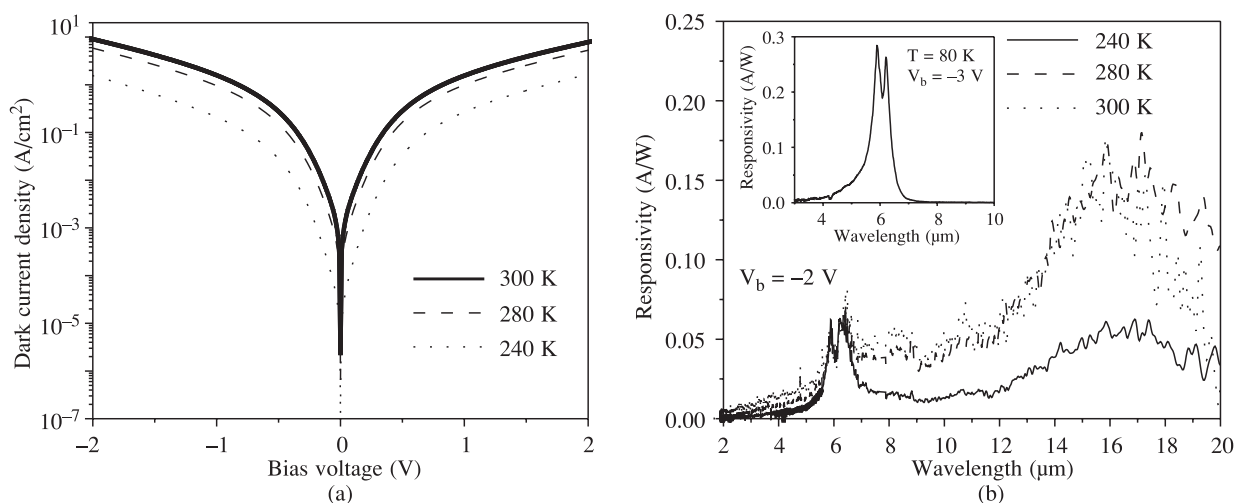

Fig. 6. The dark current density as a function of bias in the temperature range 240–300 K (a). Spectral responsivity of T-QDIP in the temperature range 240–300 K under –2 V bias. The inset shows spectral responsivity at 80 K under a bias of –3 V (b).

4. Interfacial workfunction detectors

A structure consisting of a top contact (p++ or n++) layer, an emitter (p+ or n+) layer, an undoped barrier, and a bottom contact layer (p++ or n++) can be either a homojunction or a heterojunction interfacial workfunction internal photoemission (HIWIP or HEIWIP) detector based on the material in the layers. HIWIPs have the same material in the emitters and barriers, while HEIWIPs have different material in these layers. The detection mechanism involves free carrier absorption in the emitter, followed by the internal photoemission of photoexcited carriers across the junction barrier, and then the collection of carriers by the applied electric field at the contacts. The offset between the Fermi level in the emitter layer and the valence band edge of the barrier layer gives the interfacial workfunction Δ. For HIWIPs, Δ arises due to the band gap narrowing of a highly doped emitter layer [21], while for HEIWIP, the band offset of different materials [22] also contributes to Δ. The threshold wavelength λ_c (in µm) is calculated by $1240/\Delta$, where Δ is in meV.

While recently reported dual band [1,23–25] and multiband [5,11,26,27] detectors can detect near-infrared (NIR), mid-infrared (MIR), and far-infrared (FIR) radiation, the HIWIP and HEIWIP detectors have the ability to detect a much wider range of photons, even covering the UV and FIR bands in a single structure. Both HIWIP and HEIWIP detectors [21,22] were studied as FIR detectors. Here, the focus will be on dual band detection. GaAs and Si based HIWIP for NIR/FIR and GaN/AlGaN HEIWIP for UV/FIR dual band detectors are presented in the next section.

4.1. Device structures

Figure 7(a) shows the schematic diagram of a HIWIP/ HEIWIP structure as processed. The emitter is doped, while the barrier is undoped. Highly doped layers are used for top and bottom contacts. The top contact and a part of the emitter layer were etched out in order to allow front side illuminations. The layer parameters (thickness and doping level) of the sample were confirmed by secondary ion mass spectrometry (SIMS). The mesas have different sizes of optical windows and the spectral measurements were carried out on a mesa showing the best dark current characteristics. The GaAs HIWIP structure was grown by metal organic chemical vapour deposition (MOCVD) technique at 610°C on a semi-insulating GaAs (100) substrate. The Si HIWIP structure was grown on Si substrate, while GaN HEIWIP structure was grown by MOCVD on sapphire substrate. The parameters corresponding to each layer for all the structures are given in Table 1.

The band diagram of the HIWIP/HEWIP structures is shown in Fig. 7(b). The photons (UV/NIR) with energy above the band gap (Δ_1) are absorbed in the barrier and generate an electron-hole pair. The electron-hole pairs generated in the emitter would have to undergo internal photoemission before being collected. This process is the same as for carriers generated by intraband transition in the emitter. Due to this, they would have the same threshold as for pairs generated in the barriers. Incident photons with energy below the band gap are absorbed in the emitter layer, and photoexcited carriers (free carrier absorption) then undergo internal photoemission across the barrier. The interband threshold is determined by Δ_1, while the interfacial workfunction (Δ_2) determines the FIR threshold. The photoexcited carriers are finally swept out of the active region by the applied electric field and collected at the contact. The detector was characterized by current-voltage (IV) and spectral responsivity measurements from 4.6 K up to the maximum possible temperature. The spectra were obtained using a FTIR spectrometer with three beam splitters. The calibration of spectra was done by using a spectrum obtained with a Si composite bolometer with the same combination of optical components. Since the detector responds in both bands under similar conditions, it is not tunable without exterior optical filtering.
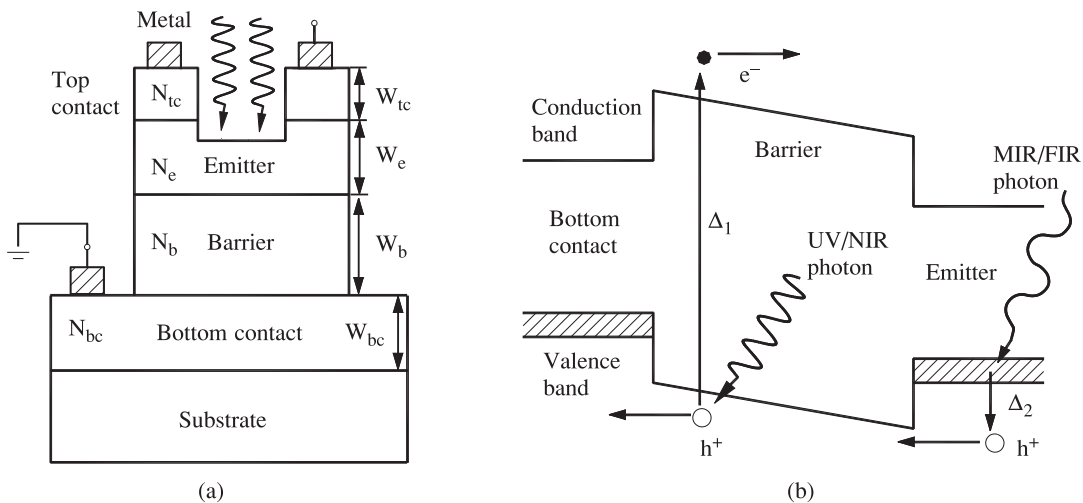

Fig. 7. Schematic of a HIWIP/HEIWIP dual-band detector after processing. A window on the top of the device is made for front side illumination (a). The band diagram of a p-type HIWIP/HEIWIP dual-band detector indicating both interband and intraband transitions leading to UV/NIR and MIR/FIR responses, depending on the material (b).

Table 1. The layer thickness (W), and the doping concentration (N) of the bottom contact (bc), barrier(b), emitter(e), and top contact (tc), respectively, for three structures. The barriers of the Si HIWIP, and GaN/AlGaN HEIWIP structures are undoped. The emitter of the GaN/AlGaN HEIWIP acts as the top contact.

Material system	Structure type	W_{bc} (μm)	N_{bc} (10^{19}cm^{-3})	W_b (μm)	N_b (10^{17}cm^{-3})	W_e (nm)	N_e (10^{18}cm^{-3})	W_{tc} (nm)	N_{tc} (10^{19}cm^{-3})
GaAs	HIWIP	1	2.0	1	1.8	200	15	120	5.3
Si	HIWIP	1	1–1.5	1	–	200	2–3	100	1–1.5
GaN/AlGaN	HEIWIP	0.7	0.5	0.6	–	200	5	–	–

4.2. NIR/FIR dual band detection

A GaAs based HIWIP structure with a p-doped emitter, undoped barrier, and heavily doped top and bottom contacts, with the parameters given in Table 1, was characterized. The NIR spectral response due to interband transitions of carriers in the GaAs barrier layer is shown in Fig. 8(a). The solid line represents the experimental curve under 100 mV reverse (top contact is negative) bias, while the dashed line represents the calculated curve based on a model [28] in which the absorption coefficient for interband transition was calculated using a permittivity model [29]. With the band gap in GaAs being 1.51 eV, the threshold wavelength observed at 0.82 μm confirms the interband transition in GaAs. The oscillations seen in the NIR region diminish with the applied electric field and the temperature. As shown in the inset to Fig. 8(a), the small peak at 0.819 μm (1.514 eV) is due to excitons [30] in GaAs, and the amplitude increases with increasing bias.

The spectral responsivity curves due intraband measured from 4.6 to 20 K are shown in Fig. 8(b). The response due to intraband transition is observed up to 70 μm with a strong dependency on the temperature. Δ decreases with the applied bias [21] giving rise to an increasing

threshold with bias. Δ of 18.4 meV corresponding to 67.5 μm threshold at 0.20 kV/cm field, and similarly, Δ of 16.5 meV giving 75 μm threshold at 0.50 kV/cm field have been confirmed [31] based on both responsivity and Arrhenius plots.

The oscillations in the MIR region observed are due to Fabry-Perot interference arising from the 1 μm thick GaAs barrier layer in the device structure. The sharp drop around 37 μm is due to the reststrahlen band of GaAs. The two peaks at 57 and 63 μm are due to transitions of hydrogenic impurity atoms in the barrier region from the impurity ground state to the excited states [28]. These transitions show a strong bias dependence due to the fact that the carriers excited to upper states must undergo tunnelling through the barrier, formed by the Coulomb potential of the acceptors, with the support of the external applied field.

An optimum responsivity of ~8 A/W and a detectivity of ~6×10^9 Jones were obtained at 0.8 μm for interband response, while a responsivity of ~7 A/W and a detectivity of ~5×10^9 Jones were reported at 57 μm, under 100-mV reverse bias at 20 K. The responsivity of the 63-μm and 57-μm peaks show a strong dependence with the temperature, and the 63-μm peak is dominant at higher temperatures. This is caused presumably by the increased rate of
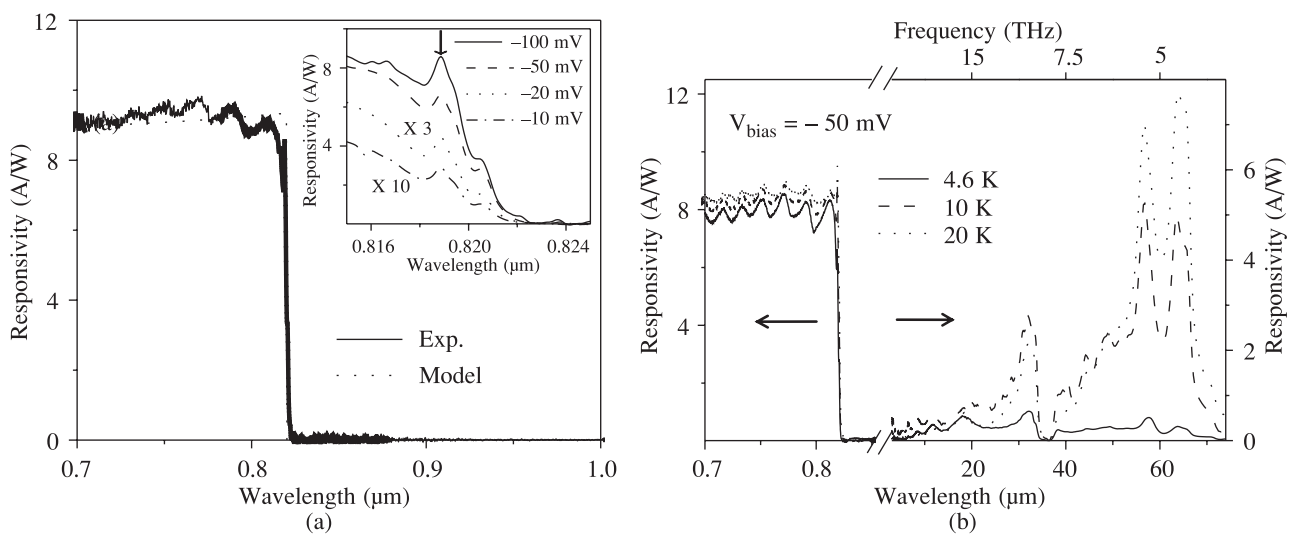

Fig. 8. The interband response fitted with a model for 100 mV reverse bias. The inset shows the bias dependence of the exciton peak at the threshold end of the experimental response curve. The two curves for 10 and 20 mV reverse bias have been multiplied by 10 and 3 for clarity (a). Interband and intraband responses at different temperatures at –50 mV bias. The left and right axes correspond to NIR and FIR, responsivity, and a break on wavelength axis at 2 μm has been made in order to expand the view in both regions (b).
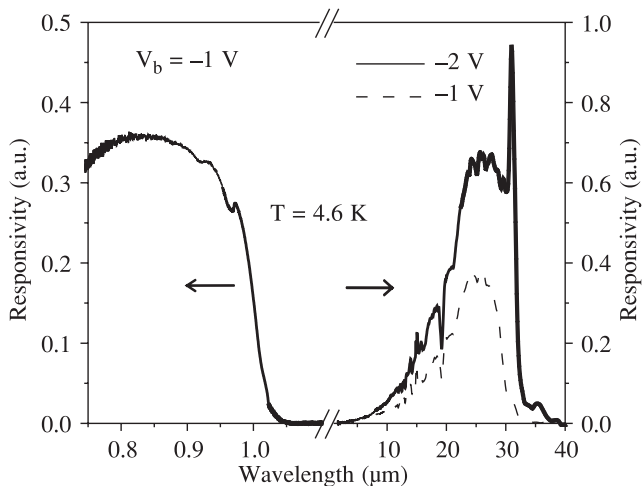
Fig. 9. The interband response of Si HIWIP dual band detector at 4.6 K under 1-V reverse bias, and intraband response under 1, and 2 V reverse bias at 4.6 K. NIR-threshold observed at ~1 µm is corresponding to the band gap of intrinsic Si. The FIR threshold is observed at ~37.5 µm. The response in both bands can be obtained up to 30 K. The left and right axes correspond to NIR and FIR, respectively, and a break on wavelength axis at 1.1 µm has been made in order to expand the view in both regions.

collecting carriers excited to the upper states from the impurity ground state at high temperature. If the rate of collection of excited carriers by the external circuit is low, the excited carriers either will relax back in to the ground state, or occupy the excited states, resulting in a high population density. At high temperature, the rate of collection of excited carriers over the barrier can be enhanced by the thermal energy, leading to enhanced responsivity.

Similar to the GaAs HIWIP detector discussed, a Si HIWIP detector having a highly p-doped Si bottom contact, an undoped Si barrier, a p-doped Si emitter, and a highly doped Si top contact has been tested. The layer parameters are given in Table 1. As shown in Fig. 9, NIR threshold at ~1 µm corresponding to interband transitions in the Si barrier, and FIR threshold at ~37.5 µm due to intraband transitions in the p-doped emitter can be observed. Similar to the GaAs HIWIP detector, the bias dependency of the sharp peak at ~30 µm proves that the corresponding transition is connected to the impurity states [28] in the structure. This detector showed a response up to 30 K in both NIR and FIR regions.

Liu *et al*. [24] reported a GaAs/AlGaAs QWIP visible/ MIR dual band detector based on interband and intersubband transitions in the structure. The well is n-doped, and a large band gap top contact layer is used to open a window for visible light. An MIR peak centred around 8.3 µm is obtained from the intersubband transitions between the two confined states in the well. Visible photons in the range 1.8–2.3 eV (0.7–0.55 µm) are absorbed in both well and barrier layers. However, the photocurrent generated from the transition from valence band of the well to the first confined state in the well has a high probability to re-

combine before being collected. Hence, the major contribution for the visible response comes from the transitions to the second confined state (close to the barrier) in the well. Touse *et al*. [26] have demonstrated a multiple step quantum well dual band detector responding in NIR and MIR regions, based on similar detection mechanism. The step quantum well is made of $In_{0.1}Ga_{0.9}As$/n-doped $In_{0.3}Ga_{0.7}As$ which in turn sandwiched in GaAs barriers. An MIR response peak at 10.3 µm is obtained due to intersubband transitions in the quantum well. An interband response is observed in the wavelength range 0.82–0.95 µm due to transitions from the valence band of the $In_{0.3}Ga_{0.7}As$ well to the second confined state in the conduction band of the well. The photons with energy above the band gap of GaAs (0.82 µm) is absorbed in the GaAs barrier layer, and this determines the lower wavelength limit of the interband response.

4.3. UV/IR HEIWIP dual band detector

A modification of the HIWIP structure with GaN/AlGaN, a solar blind UV/IR dual band structure is also feasible. UV detectors are used in numerous areas such as military, biology, and environmental research. The structure considered is grown on sapphire substrate, and n-doped GaN and undoped AlGaN are used for the emitter and the barrier, respectively. A doped GaN layer is used as the bottom contact, while the emitter itself acts as the top contact. The layer parameters are given in Table 1. A GaN/AlGaN UV detector can detect UV radiation by interband absorption in the AlGaN barrier layer. UV detectors have already been demonstrated by several groups [32–34] using GaN/AlGaN system. Intraband transitions giving rise to IR absorption in GaN/AlGaN is similar to that in GaAs/AlGaAs HEIWIP detectors [35]. Preliminary measurements in both UV and IR regions, as shown in Fig. 10, show better performance in both regions. The interband response leading to UV detection can be obtained at room temperature. The UV-threshold observed is 360 nm, and it is in good agreement with the band gap of AlGaN. The intraband threshold is observed at ~400 µm at 5.3 K, and this promotes the development of terahertz GaN detectors. Due to strong TO phonon-photon interaction and phonon absorption, a deep valley at ~18 µm in the responsivity curve of a GaN/AlGaN detector (~37 µm for GaAs/AlGaAs) is observed. Furthermore, expected results are in good agreement with the theoretical model in both UV and IR bands, and the inset to Fig. 10(b) shows the MIR response fitted with the theoretical model. The IR response with 14 µm threshold can be obtained up to 80 K. Compared to the GaAs/AlGaAs system, GaN/AlGaN has advantages in controlling the Al fraction over a wide range, and the broad continuous spectral response range.

This approach could be used to develop dualband detectors tailored to specific applications. By adjusting the material in the layers, the thresholds for the interband and intraband responses can be tailored separately. For exam-
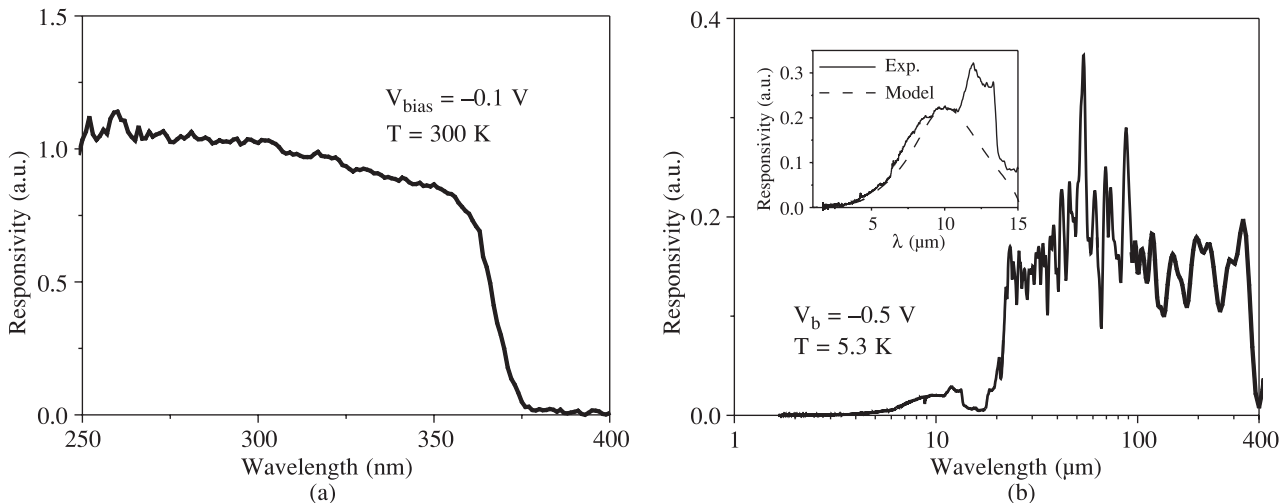
Fig. 10. UV response of GaN/AlGaN HEIWIP dual band detector, arising due to interband transitions in AlGaN barrier layer at 300 K. A UV-threshold, observed at 360 nm under 0.1 V reverse bias at 300 K, is corresponding to the band gap of $Al_xGa_{1-x}N$ with $x = 0.026$ (a). IR response with an FIR threshold of ~400 μm at 5.3 K under −0.5 V bias. The inset shows the MIR response fitted with the theoretical model (b).

ple, in an AlGaN based detector, if the Al fraction is varied in both the emitter and barrier by the same amount, the intraband threshold will not be changed while the interband threshold will change. Alternatively varying only the emitter Al fraction, the intraband threshold could be varied without changing the interband threshold. Moreover, the resonant cavity effects can be used to tailor the IR response peak to the desired wavelength. By adjusting the materials it should be possible to tune the interband threshold from the UV to NIR and the intraband threshold from the MIR to the FIR. That is, the reported dual band approach with HIWIP/HEIWIP detectors can be tested with any material such as InN, InGaN, GaN, AlGaN, and AlN. InN could give an interband response in NIR, while InGaN could respond in NIR-Visible region. A UV interband response could be expected from an AlN based detector. Also, as the response for the two processes originates at different locations, it may be possible to design a device that is capable of separately measuring both components simultaneously. Δ determines the IR threshold, and lowering the Δ will increase the dark current, resulting in a lowering of the operating temperature of the detector. In another word, any HIWIP/HEIWIP design focused on increased threshold will reduce the operating temperature. One of the possibilities to increase the operating temperature is to use the resonance tunnelling approach, in which the photocurrent is selectively collected by incorporating tunnelling barriers in to the structure. Furthermore, different design possibilities to increase the performance of the detector will be studied.

5. Conclusions

In summary, multiband photon detection covering MIR/FIR, NIR/MIR/FIR, UV/MIR, and UV/FIR has been discussed. Based on the results, the transitions leading to each peak of DWELL detectors are explained. Room temperature operation of T-QDIP is made possible by incorporating tunnelling barriers. HIWIP/HEIWIP detectors can detect NIR or UV, and MIR/FIR radiation, due to interband and intraband transitions within the structure. By adjusting the material, the threshold of the interband and intraband responses can be tailored. Based on theoretical models and experimental data, the transition leading to each bands are explained. High performances of the detectors demonstrate the potential applications where the detection in multibands is important.

Acknowledgements

References

1. A. Goldberg, P.N. Uppal, and M. Winn, "Detection of buried land mines using a dual-band LWIR/LWIR QWIP focal plane array", *Infrared Phys. & Technol.* **44**, 427 (2003).
2. B. Kochman, A.D. Stiff-Roberts, S. Chakrabarti, J.D. Phillips, S. Krishna, J. Singh, and P. Bhattacharya, "Absorption, carrier lifetime, and gain in InAs-GaAs quantum-dot infrared photodetectors", *IEEE. J. Quant. Electron.* **39**, 459 (2003).
3. H.C. Liu, M. Gao, J. McCaffrey, Z.R. Wasilewski, and S. Fafard, "Quantum dot infrared photodetectors", *Appl. Phys. Lett.* **78**, 79 (2001).
4. L. Jiang, S.S. Li, N.T. Yeh, J.I. Chyi, C.E. Ross, and K.S. Jones, "In$_{0.6}$Ga$_{0.4}$As/GaAs quantum-dot infrared photode-

tector with operating temperature up to 260 K", *Appl. Phys. Lett.* **82**, 1986–1988 (2003).

5. A. Raghavan, P. Rotella, A. Stintz, B. Fuchs, S. Krishna, C. Morath, D.A. Cardimona, and S.W. Kennerly, "High-responsivity, normal-incidence long-wave infrared (λ_p ~7.2 µm) InAs/In$_{0.15}$Ga$_{0.85}$As dots-in-a-well detector", *Appl. Phys. Lett.* **81**, 1369 (2002).

6. B. Aslan, H.C. Liu, M. Korkusinski, S.J. Cheng, and P. Hawrylak, "Response spectra from mid- to far-infrared, polarization behaviors, and effects of electron numbers in quantum-dot photodetectors", *Appl. Phys. Lett.* **82**, 639 (2003).

7. Z. Ye and J.C. Campbell, "InAs quantum dot infrared photodetectors with In$_{0.15}$Ga$_{0.85}$As strain-relief cap layers", *J. Appl. Phys.* **92**, 7462–7468 (2002).

8. J. Phillips, K. Kamath, and P. Bhattacharya, "Far-infrared photoconductivity in self-organized InAs quantum dots", *Appl. Phys. Lett.* **72**, 2020 (1998).

9. S. Maimon, E. Finkman, and G. Bahir, "Intersublevel transitions in InAs/GaAs quantum dots infrared photodetectors", *Appl. Phys. Lett.* **73**, 2003 (1998).

10. D. Pan, E. Towe, and S. Kennerly, "Normal-incidence intersubband (In,Ga)As/GaAs quantum dot infrared photodetectors", *Appl. Phys. Lett.* **73**, 1937 (1998).

11. S. Krishna, S. Raghavan, G. von Winckel, A. Stintz, G. Ariyawansa, S.G. Matsik, and A.G.U. Perera, "Three-colour (λ_{p1} ~3.8 µm, λ_{p2} ~8.5 µm, and λ_{p3} ~23.2 µm) InAs/InGaAs quantum-dots-in-a-well detector", *Appl. Phys. Lett.* **83**, 2745–2747 (2003).

12. G. Ariyawansa, A.G.U. Perera, G.S. Raghavan, G. von Winckel, A. Stintz, and S. Krishna, "Effect of well width on three colour quantum dots-in-a-well infrared detectors", *IEEE Photon. Technol. Lett.* **17**, 1064 (2005).

13. B.F. Levine, "Quantum-well infrared photodetectors", *J. Appl. Phys.*, **74**, R1–R81 (1993).

14. A. Amtout, S. Raghavan, P. Rotella, G. v. Winckel, A. Stintz, and S. Krishna, "Theoretical modeling and experimental characterization of InAs/InGaAs quantum dots in a well detector", *J. Appl. Phys.* **96**, 3782–3786 (2004).

15. S.V. Bandara, S.D. Gunapala, J.K. Liu, E.M. Luong, J.M. Mumolo, W. Hong, D.K. Sengupta, and M.J. McKelvey, "10–16 µm broad band quantum well infrared photodetector", *Appl. Phys. Lett.* **72**, 2427 (1998).

16. A.G.U. Perera, W.Z. Shen, S.G. Matsik, H.C. Liu, M. Buchanan, and W.J. Schaff, "GaAs/AlGaAs quantum well photodetectors with a cutoff wavelength at 28 µm", *Appl. Phys. Lett.* **72**, 1596–1598 (1998).

17. P. Bhattacharya, X.H. Su, S. Chakrabarti, G. Ariyawansa, and A.G.U. Perera, "Characteristics of a tunnelling quantum dot infrared photodetector operating at room temperature", *Appl. Phys. Lett.* **86**, 191106 (2005).

18. J. Urayama, T.B. Norris, J. Singh, and P. Bhattacharya, "Observation of phonon bottleneck in quantum dot electronic relaxation", *Phys. Rev. Lett.* **86**, 4930 (2001).

19. E. Kim, A. Madhukar, Z. Ye, and J.C. Campbell, "High detectivity InAs quantum dot infrared photodetectors", *Appl. Phys. Lett.* **84**, 3277 (2004).

20. H. Jiang and J. Singh, "Strain distribution and electronic spectra of InAs/GaAs self-assembled dots: An eight-band study", *Phys. Rev.* **B56**, 4696–4701 (1997).

21. W.Z. Shen, A.G.U. Perera, H.C. Liu, M. Buchanan, and W.J. Schaff, "Bias effects in high performance GaAs homojunction far-infrared detectors", *Appl. Phys. Lett.* **71**, 2677–2679 (1997).

22. D.G. Esaev, M.B.M. Rinzan, S.G. Matsik, and A.G.U. Perera, "Design and optimization of GaAs/AlGaAs heterojunction infrared detectors", *J. Appl. Phys.* **96**, 4588–4597 (2004).

23. H.C. Liu, P.H. Wilson, M. Lamm, A.G. Steele, Z.R. Wasilewski, J. Li, M. Buchanan, and J.G. Simmonsa, "Low dark current dual band infrared photodetector using thin AlAs barriers and G-X mixed intersubband transition in GaAs quantum wells", *Appl. Phys. Lett.* **64**, 475 (1994).

24. H.C. Liu, C.Y. Song, A. Shen, M. Gao, Z.R. Wasilewski, and M. Buchanan, "GaAs/AlGaAs quantum-well photodetector for visible and middle infrared dual-band detection", *Appl. Phys. Lett.* **77**, 2437 (2000).

25. M.P. Touse, G. Karunasiri, K.R. Lantz, H. Li, and T. Mei, "Near- and mid-infrared detection using GaAs/In$_x$Ga$_{1x}$As/ In$_y$Ga$_{1y}$As multiple step quantum wells", *Appl. Phys. Lett.* **86**, 093501-1 (2005).

26. K.K. Choi, B.F. Levine, C.G. Bethea, J. Walker, and R.J. Malik, "Infrared photoelectron tunnelling spectroscopy of strongly coupled quantum wells", *Phys. Rev.* **B39**, 8029 (1989).

27. S. Chakrabarti, X.H. Su, P. Bhattacharya, G. Ariyawansa, and A.G.U. Perera, "Characteristics of a multicolour InGaAs–GaAs quantum-dot infrared photodetector", *IEEE Photon. Technol. Lett.* **17**, 178–180 (2005).

28. D.G. Esaev, M.B.M. Rinzan, S.G. Matsik, A.G.U. Perera, H.C. Liu, B.N. Zvonkov, V.I. Gavrilenko, and A.A. Belyanin, "High performance single emitter homojunction interfacial work function far infrared detectors", *J. Appl. Phys.* **95**, 512–519 (2004).

29. S. Adachi, "Refractive indices of III–V compounds: Key properties of InGaAsP relevant to device design", *J. Appl. Phys.* **53**, 5863 (1982).

30. M.D. Sturge, "Optical absorption of gallium arsenide between 0.6 and 2.75 eV", *Phys. Rev.* **127**, 768 (1962).

31. G. Ariyawansa, M.B.M. Rinzan, D.G. Esaev, S.G. Matsik, G. Hastings, A.G.U. Perera, H.C. Liu, B.N. Zvonkov, and V.I. Gavrilenko, "Near- and far-infrared p-GaAs dual-band detector", *Appl. Phys. Lett.* **86**, 143510–143513 (2005).

32. F. Binet, J.Y. Duboz, E. Rosencher, F. Scholz, and V. Harle, "Mechanisms of recombination in GaN photodetectors", *Appl. Phys. Lett.* **69**, 1202 (1996).

33. S.K. Zhang, W.B. Wang, I. Shtau, F. Yun, L. He, H. Morkoc, X. Zhou, M. Tamargo, R.R. Alfano, "Backilluminated GaN/AlGaN heterojunction ultraviolet photodetector with high internal gain", *Appl. Phys. Lett.* **81**, 4862 (2002).

34. E. Monroy, F. Omnes, and F. Calle, "Wide-bandgap semiconductor ultraviolet photodetectors", *Semicond. Sci. Technol.* **18**, R33–R51 (2003).

35. S.G. Matsik, M.B.M. Rinzan, D.G. Esaev, A.G.U. Perera, H.C. Liu, and M. Buchanan, "20 µm cutoff heterojunction interfacial work function internal photoemission detectors", *Appl. Phys. Lett.* **84**, 3435–3437 (2004).